Near-wall heat transfer phenomena during bubble growth in nucleate boiling

Cassiano Tecchio, Corentin Le Houedec, Benjamin Cariteau, Guillaume Bois, Elie Saikali, Gilbert Zalczer, Pere Roca I Cabarrocas, Pavel Bulkin, Jérôme Charliac, Simon Vassant, et al.

NEAR-WALL HEAT TRANSFER PHENOMENA DURING BUBBLE GROWTH IN NUCLEATE BOILING

Cassiano Tecchio[a,*], Corentin Le Houedec[a], Benjamin Cariteau[a], Guillaume Bois[a], Elie Saikali[a], Gilbert Zalczer[b], Pere Roca i Cabarrocas[c], Pavel Bulkin[c], Jérôme Charliac[c], Simon Vassant[b], Vadim S. Nikolayev[b]
[a]Université Paris-Saclay, CEA, STMF, 91191 Gif-sur-Yvette Cedex, France
[b]Université Paris-Saclay, CEA, SPEC, CNRS, 91191 Gif-sur-Yvette Cedex, France
[c]Institut Polytechnique de Paris, Ecole polytechnique, LPICM, CNRS, 91120 Palaiseau, France
*cassiano.tecchio@cea.fr

Abstract. We experimentally investigate the near-wall heat transfer at single bubble growth in nucleate saturated pool boiling of water at atmospheric pressure. Our focus is on the evaporation of the micro-metric thin film of liquid (microlayer) that is formed between the heating wall and the bubble. Synchronous and simultaneous measurements of the microlayer thickness, wall temperature and bubble macroscopic shape are performed by white light interferometry, infrared thermography and side-wise shadowgraphy, respectively. We measure the wall temperature of an ITO heating film through a transparent to the infrared waves porthole. The heating is provided by an infrared laser. The wall heat flux is numerically reconstructed by using the experimental wall temperature data. We reveal a temporal rise of the thermal resistance of the liquid-vapor interface during the microlayer evaporation, which corresponds to a decrease of the accommodation coefficient. We attribute it to the progressive accumulation of impurities at the interface during evaporation.

Keywords: microlayer, contact line, boiling, heat transfer

1. INTRODUCTION

During the growth of bubbles on a heated wall, a thin layer of liquid having a thickness of a few μm (known as microlayer) (Jung & Kim, 2014; Guion, *et al*., 2018; Urbano, *et al*., 2018) can be formed between the wall and the liquid-vapor interface of the bubble, as illustrated in Fig. 1. A dry spot is also formed on the wall, establishing a triple liquid-vapor-solid contact line. The wall heat flux is very low in the dry spot, resulting in a local rapid temperature increase. Unlike the dry spot, the microlayer acts as a heat transfer bridge between the wall and the liquid-vapor interface of the bubble, promoting heat fluxes of the order of MW/m^2 that cool down the heater and promote the microlayer evaporation. Two thermal resistances act to decreasing the microlayer evaporation rate. The first is the conductive through the film thickness, which is well determined by measuring the microlayer thickness. The second is the interfacial thermal resistance at the liquid-vapor interface. The issue of the interfacial thermal resistance in water remains an open question in the literature (Eames, *et al*., 1997; Giustini, *et al*., 2016). In this work, we perform experiments on single bubble growth at nucleate boiling at atmospheric pressure to investigate the near-wall heat transfer phenomena, in particular, to study the interfacial thermal resistance in the microlayer.

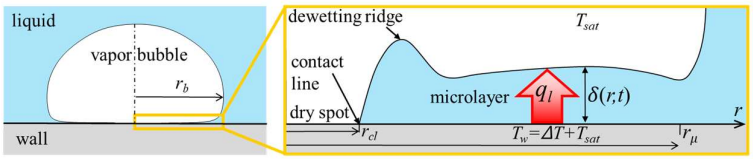

Figure 1. Schematics of the microlayer profile underneath a bubble.

2. HEAT TRANSFER IN MICROLAYER

Let us consider again the schematics of the near-wall region at bubble growth represented in Fig. 1. The wall temperature T_w surpasses the temperature T_{sat} of the vapor at saturation by an amount ΔT called the wall superheating which will thus promote a heat flux in the microlayer. Note that T_w and thus ΔT are both functions of position at the wall surface and of time t. Since the microlayer is thin, one can assume a locally quasi-stationary linear temperature profile through the microlayer of local thickness δ. The heat flux through it reads

$$q_l = \frac{\Delta T}{\delta / k_l + R^i}, \tag{1}$$

where k_l is the liquid conductivity and R^i represents the interfacial thermal resistance. By neglecting both the heat flux into the vapor (because of its small conductivity) and the radial flow in the microlayer (because of high viscous stresses) (Nikolayev, 2022), one obtains

$$L\rho_l \frac{\partial \delta}{\partial t} = -\frac{\Delta T}{\delta / k_l + R^i}, \tag{2}$$

where ρ_l is the liquid density and L the latent heat of vaporization. One can see that δ is a decreasing function of *t* thus representing a thinning of microlayer due to evaporation. Vapor is produced at the liquid-vapor interface along the whole microlayer extent. This explains why the relative contribution of microlayer evaporation to the overall bubble growth can be important (Myers, *et al*., 2005; Utaka, *et al*., 2014; Jung & Kim, 2014; Chen & Utaka, 2015; Utaka, *et al*., 2018).

As expressed in Eq. (1), an important parameter during microlayer evaporation is R^i. It acts to decrease q_l and so the mass evaporation flux at the liquid-vapor interface. In the Schrage kinetic theory of gases (Nikolayev, 2022), it is related to a limitation associated with the finiteness of velocity of the vapor molecules leaving the interface during evaporation. Its value is

$$R^i = \frac{2-f}{2f} \frac{T_{sat}\sqrt{2\pi \Re_g T_{sat}}}{L^2 \rho_v}, \tag{3}$$

where $\Re_g$ is the specific gas constant and ρ_v is the vapor density. The accommodation coefficient *f* characterizes the ability of molecules to leave the interface. For water at 100°C and 1 bar, $R^i|_{f=1} \equiv R^i_{theo} = 0.064$ μKm^2/W; this value is called hereafter theoretical.

In practice, the issue of the accommodation coefficient in water is important but highly controversial, being under active discussion over the last years (Giustini, *et al*., 2016; Giustini, *et al*., 2019; Bureš & Sato, 2022; Torres, *et al*., 2024). Early experimental results (Eames, *et al*., 1997; Marek & Straub, 2001) show that the value of *f* exhibits a large uncertainty ranging from 1 down to 0.01, so R^i can be much larger than R^i_{theo}. By referring to the single bubble growth experiments of Bucci (2020), Bureš & Sato (2022) argue that *f* =0.03. On the other hand, some other results (Giustini, *et al*., 2016) show that *f* value may not be constant over time and space while the microlayer evaporates, ranging from 0.1 down to 0.02.

In this work, we investigate experimentally the single bubble growth in pool boiling by using advanced optical techniques to solve these issues. We first characterize the near-wall heat transfer by measuring δ and ΔT. The wall heat flux q_l is recovered by using the experimental wall temperature distribution. R^i can then be determined via Eq. (1). Finally, the accommodation coefficient is discussed.

3. EXPERIMENTS

The experimental setup is schematized in Fig. 2. The boiling cell consists of a water pool at atmospheric pressure surrounded by a temperature-regulated jacket. The heater consists of a ~1 μm thick indium-tin-oxide (ITO) film deposited on a magnesium fluoride (MgF_2) optical porthole. MgF_2 is transparent to both visible and infrared (IR) light whereas ITO is transparent to visible but opaque to IR. The growth of a single bubble at a time is produced by heating up the ITO film locally with a 1.2 μm wavelength IR continuous laser beam of ~1.5 mm diameter. High-speed (4000 fps) and high-resolution optical techniques are employed. The bubble macroscopic shape (Fig. 2a) is observed by sidewise shadowgraphy. The microlayer thickness δ is measured by white light interferometry (WLI). A LED light source produces a collimated beam of white light that is sent towards the bubble from below with perpendicular incidence to the heater. The light reflected at the interfaces MgF_2/ITO, ITO/microlayer and microlayer/vapor produces a colored fringe pattern which is directed towards a spectrometer by a visible light beam splitter. At the entrance of the spectrometer, a slit defines a scanning line on the heater. The fringe pattern is then dispersed into wavelength λ by a diffraction grating inside the spectrometer, producing a spectral fringe map (Fig. 2b). In Fig. 2b, the ordinate corresponds to λ and abscissa, to the physical position *r* on the heater along the scanning line. The microlayer thickness distribution $\delta(r)$ is determined by comparing the experimental spectral intensity with a two beam interference model (Tecchio, 2022). From Fig. 2b one can also obtain the dry spot (contact line) radius r_{cl} and the microlayer radius r_μ. The diffraction grating can also be replaced by a mirror to observe the dry spot and microlayer extents over the heater as shown in Fig. 2c.

The infrared thermography (IRT) is used to measure the temporal evolution of the wall temperature distribution $T_w(x,y,t)$ (Fig. 2d). We use a custom-made multilayer visible-IR light beam splitter. It is transparent to visible light but

reflective to IR waves. It is positioned between the boiling cell and the visible light beam splitter to reflect the IR radiation emitted by the ITO to the fast IR camera sensitive in the range 3-5 µm. The temperature is deduced from the recorded intensity thanks to the preliminary pixel-wise calibration (Tecchio, 2022).

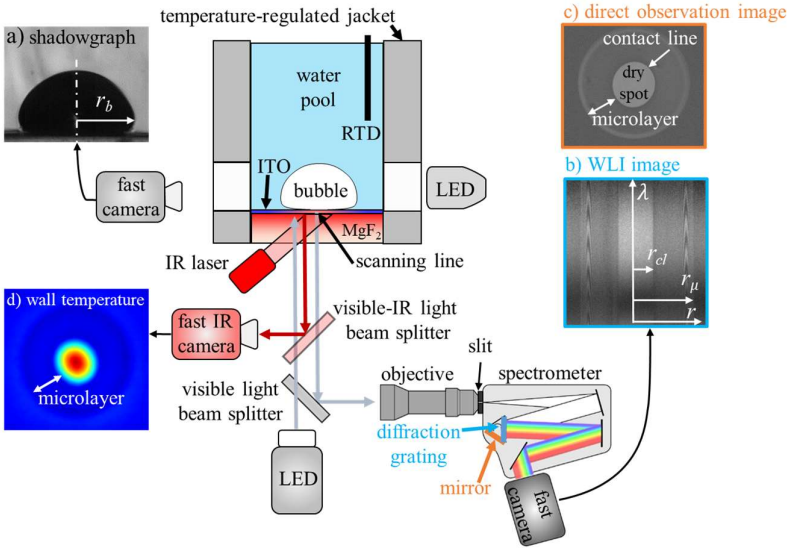

Figure 2. Schematics of the experimental setup.

4. RECONSTRUCTED HEAT FLUX

One can reconstruct the wall heat flux q_l (Fig. 1) by solving the energy balance in the ITO film. It yields the expression (Tecchio, *et al.*, 2024)

$$q_l = j_0 + q_p + \underbrace{hk_w\left(\frac{\partial^2 T_w}{\partial x^2}+\frac{\partial^2 T_w}{\partial y^2}\right)}_{q_d} - \underbrace{h\rho_w c_w \frac{\partial T_w}{\partial t}}_{q_a}, \tag{4}$$

where j_0 is the equivalent surface heat flux induced externally by the IR laser and q_p is the heat flux towards the porthole (MgF_2). We determine j_0 by measuring the intensity distribution of the same laser measured with the IR beam profiler BladeCam2-HR in a dedicated optical setup. To find j_0, the intensity should be multiplied by the ITO absorption that is measured separately by Fourier-Transform IR Spectroscopy (FTIR) (Tecchio, 2022). Both auxiliary experiments are performed at the same incidence angle as the main experiment. The only yet undefined quantity in the right-hand side (RHS) of Eq. (4) is the heat flux q_p at the porthole upper surface. q_p is obtained by solving numerically the transient heat diffusion in the MgF_2 (Tecchio, *et al.*, 2024). The third and fourth terms in the RHS of Eq. (1) represent the heat diffusion (q_d) and accumulation in the ITO (q_a), respectively. They are obtained from the transient 2D distribution of T_w measured by IRT. *h* is the ITO thickness measured *in-situ* by WLI with a bare MgF_2 (without ITO) and the boiling cell empty. ρ_w, c_w and k_w stand for the density, specific heat and thermal conductivity of the ITO film. The wall temperature T_w is given by the IRT. Equation (4) is valid everywhere on the wall, including the dry spot and the microlayer, and at any time moment.

The uncertainties of the experimentally measured quantities are provided in table 1.

Table 1. Uncertainties on measurements.

r_{cl}, r_b	±0.07 mm
r_μ	±0.1 mm
h, δ	±15 nm
T_w , ΔT	±0.5 K
q_l	±0.04 MW/m^2

5. RESULTS

5.1 Bubble nucleation, growth and departure

Figure 3a shows the time evolution of the wall superheating $\Delta T = T_w - T_{sat}$ obtained with IRT at the bubble nucleation point. The displayed time lapse comprises a few nucleation cycles with the highlighted growth time interval of a bubble, given by the time between bubble nucleation and departure from the wall. Its duration is $t_d \approx 19.5$ ms. It is zoomed in Fig. 3b. The boiling cycles are periodic with 248 ms between two consecutive bubble nucleation events. As the ITO surface has only nanoscale roughness (Tecchio, 2022), the ΔT required to overcome the nucleation energy barrier and thus initiate the bubble growth is high, ~32 K. The average heat flux applied to the ITO is also much higher than in previous works on microlayer, about 1.1 MW/m^2 calculated as the absorbed laser power divided by the beam area. ΔT drops sharply at nucleation thanks to the wall heat removal promoted by the latent heat of vaporization. However, the rapid dry spot formation results in a sharp increase of ΔT . This increase is slowed down after a few ms because of the radial heat diffusion towards the contact line, where strong evaporation occurs. At bubble departure from the wall, ΔT decreases due to the wall rewetting by the colder liquid from the bulk. Thanks to the periodicity of nucleation cycles evident in Fig. 3a, one can analyze the near-wall heat transfer phenomena during a single growth time interval.

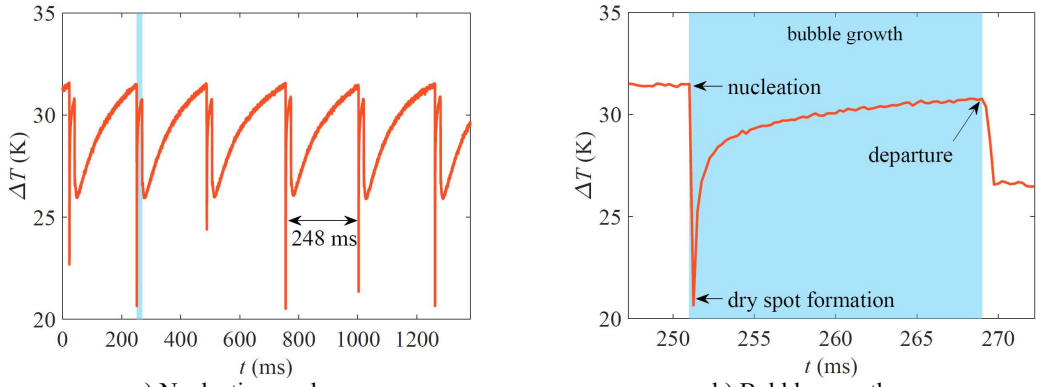

a) Nucleation cycles. b) Bubble growth.

Figure 3. Wall superheating evolution at the center of the bubble. The shaded zone indicates the bubble growth period.

5.2 Bubble, dry spot and microlayer radii

The time evolution of the bubble, microlayer and dry spot radii is shown in Fig. 4a from nucleation to departure. From now on, t = 0 ms is assumed to correspond to the moment just before nucleation. The bubble departs from the wall at $t = t_d$. For $t \leq 1$ ms, the dynamics of the bubble and microlayer radii is similar thanks to the inertial bubble expansion, which results in a nearly hemispherical bubble shape. The microlayer radius attains 90% of its maximum (~2mm) within the first 10% of bubble growth period. It vanishes at t = 12.5 ms, where r_{cl} and r_μ coincide. Prior to its disappearance, r_{cl} increases due to the wall dewetting whereas r_μ decreases because buoyancy forces push the bubble upwards. The microlayer disappearance is therefore the result of the microlayer shortening and not because of its thinning caused by evaporation (Urbano, *et al*., 2018; Jung & Kim, 2014). The microlayer exists for $0 \leq t \leq 12.5$ ms and its evaporation contributes to the overall bubble growth. For the remaining bubble lifetime, the microlayer does not exist anymore and the contact-line evaporation regime (according to the classification given by Bureš & Sato, (2021)) occurs instead.

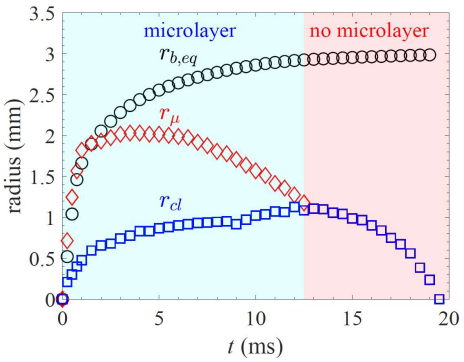

a) Our data obtained with localized heating.

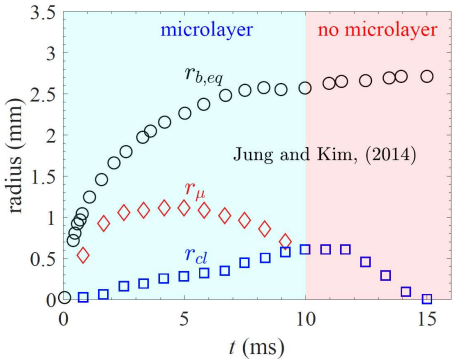

b) The data of Jung & Kim (2014) obtained with uniform heating.

Figure 4. Experimental temporal evolution of the characteristic radii.

The dynamics of the radii shown in Fig. 4a is also qualitatively similar to that obtained in other experiments (Jung & Kim, 2014; Surtaev, *et al*., 2018). The data of Jung & Kim (2014) are reproduced in Fig. 4b. It can be noticed that r_μ is roughly two times larger for the localized heating case. This is a result of strong inertial forces acting during early stage of bubble growth, which is specific to this case. During the microlayer existence, r_{cl} has a linear increase in the case of uniform heating (Fig. 4b). With the localized heating (Fig. 4a), r_{cl} grows faster for $t \leq 2.5$ ms and then slows down. The contact line receding speed becomes then constant until microlayer disappears. The reason for this is that the speed is controlled by the wall superheating at the contact line $\Delta T_{cl} = T_{w,cl} - T_{sat}$ (Fourgeaud, *et al*., 2016; Zhang & Nikolayev, 2022). At the early stages of bubble growth ($t \leq 2.5$ ms), the contact line is located on the hot spot of the laser heating where ΔT_{cl} is high. As the contact line recedes, it moves away from the hot spot, where ΔT_{cl} is lower so the contact line speed decreases.

5.3 Microlayer dynamics

The microlayer thickness profile is shown in Fig. 5. It could be recovered in the microlayer part where the fringe pattern is visible. The microlayer is also not resolved for $t < 1.25$ ms because of so fast inertial dynamics that the fringes become smeared. At $t = 7.5$ ms and until the microlayer disappearance at 12.5 ms, the extent of the fringe pattern becomes so small that its post-processing is no longer possible. This indicates strong interfacial slopes caused probably by the dewetting ridge growth. Therefore, the experimental microlayer profile can only be determined when r_μ in Fig.4a is at the plateau (~2mm), which corresponds to the time period between 1.25 and 7.5 ms. The microlayer is slightly bumped and attains a maximum thickness at r~1.6 mm. Due to the microlayer evaporation, the thickness decreases over time but its ''bumped'' shape persists.

With the help of an approach based on the extended lubrication theory (Zhang & Nikolayev, 2022), the entire microlayer profile could be simulated numerically (Tecchio, *et al*., 2024). It is briefly discussed here. It consists of two regions: a dewetting ridge located near the contact line followed by a flatter and wider region, as illustrated in Fig. 1. The ridge features very high slopes; it is formed because high viscous stresses in the flat part of the microlayer prevent the inflow. The liquid gets accumulated near the contact line while it recedes thus forming a ridge. However, WLI has a strong limitation on the measurable interfacial slope θ related to the finiteness of optical resolution (Tecchio, *et al*., 2024). The fringes are visible over only a portion of microlayer where $|\theta| < \theta_{max}$. $\theta_{max} \sim 0.4^\circ$ in the present installation. Therefore, the experimental data of Fig. 5 could only be obtained in a flatter part where the contact line motion has no effect.

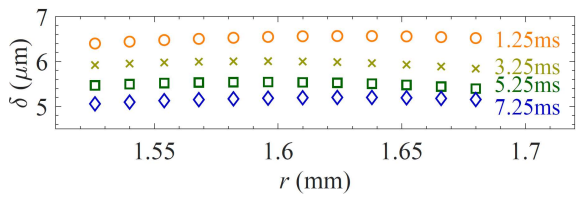

Figure 5. Microlayer profile.

5.4 Wall temperature

Figures 6a and 6b show $\Delta T(x,y)$ for t = 0 ms and t = 6.25 ms, respectively. In these figures, $(x=0, y=0)$ corresponds to the point on the wall where the bubble nucleation occurs. In Fig. 6a, one can understand the temperature distribution as a combination of the heat generation in the ITO provided by the IR laser heating, the heat diffusion towards the porthole and radial in the ITO and the convection into the liquid pool. In Fig. 6b, the presence of dry spot and microlayer change significantly this distribution. Therefore, we use $\Delta T(x,y,t=0)$ as a reference to address how the microlayer and dry spot modify $\Delta T(x,y,t)$. For the sake of simplicity and due to nearly radial symmetry of the temperature distribution on the wall, as one can observe in Figs. 6a,b, the spatial distribution of ΔT can be studied by profiles of $\Delta T(x,t)$ at $y=0$.

Figures 7a,b depict the wall superheating at the early stages of bubble growth. In Fig. 7a, one can easily identify both the dry spot and the microlayer. The evaporation of the latter can be considered stationary because the depth of temperature penetration into the microlayer is 6.5 µm during 0.25 ms, which is the time between two consecutive frames. Therefore, the heat diffuses from the wall throughout the whole microlayer thickness rapidly, thus promoting an effective and fast heat removal from the wall. As a result, $\Delta T(x,t=0.25\text{ms})$ deviates from $\Delta T(x,t=0)$ for $|x| \le r_\mu$, i.e. inside the whole microlayer extent. The dry spot edges (i.e. the contact line positions) can be easily identified as local ΔT minima caused by strong evaporation. ΔT distribution is nonmonotonous inside the microlayer (Fig. 7a). This is a combined result of evaporation and nonuniform heating by the IR laser. While the high wall heat removal rate near the contact line works to decrease ΔT, the IR laser heating tends to increase it. The laser heating is maximum inside the dry spot thus producing high temperature gradients on the wall in this region. As a result, we identify the dry spot radius $x = r_{cl}$ by two points where ΔT increases sharply. These points correspond to the contact line position.

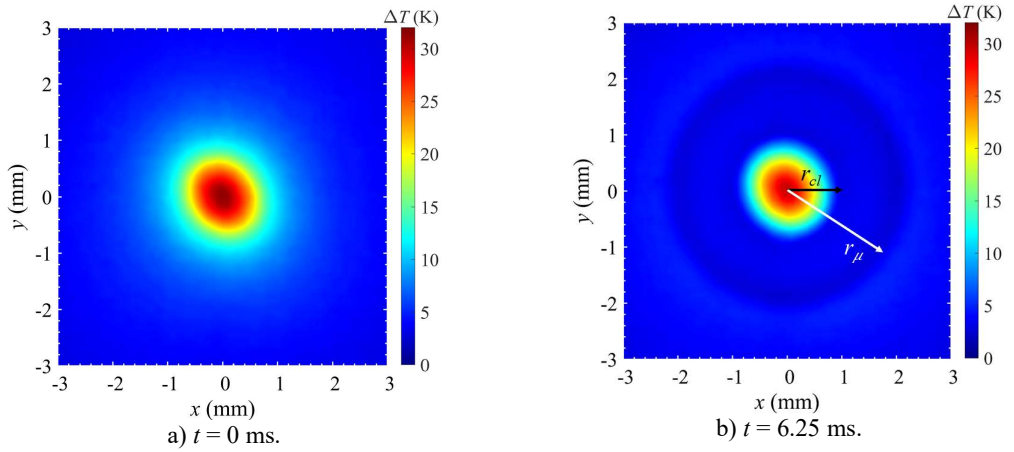

a) t = 0 ms. b) t = 6.25 ms.

Figure 6. Superheating ΔT distribution on the wall.

As one can observe in Figs. 7, $\Delta T(t)$ is a decreasing function along the whole extent of the microlayer as the bubble grows. In particular, at t = 1.25ms (Fig. 7b), $\Delta T(x)$ is nearly uniform inside the microlayer thus conforming the effective wall cooling along its extent. Over the dry spot, the temperature profile follows approximately the shape of that at t = 0. As the microlayer approaches its full development (at t =1.25 ms), the changes in ΔT along the dry spot become minor. This is a result of the effective wall heat removal at the contact line and also throughout the whole microlayer extent.

Figure 7c shows the ΔT distribution after the microlayer is fully developed. Here, its variation is different. ΔT inside the microlayer is lower than at its periphery. As a result, heat diffuses inwards. The point where the profiles for t = 0 and 6.25 ms start to deviate from each other no longer corresponds to r_μ. Instead, at r_μ = 2 mm and at r_{cl} = 1 mm, we have two ΔT minima; the region between them corresponds to the microlayer. The minima at $x = \pm 2$ mm correspond to the cold ring on the x-y map of Fig. 6b. When the microlayer disappears at t = 12.5 ms in Fig. 7d, the second pair of minima of ΔT at $x = \pm 2$ mm disappears. For t > 12.5 ms, the temperature at the contact line increases due to the absence of microlayer.

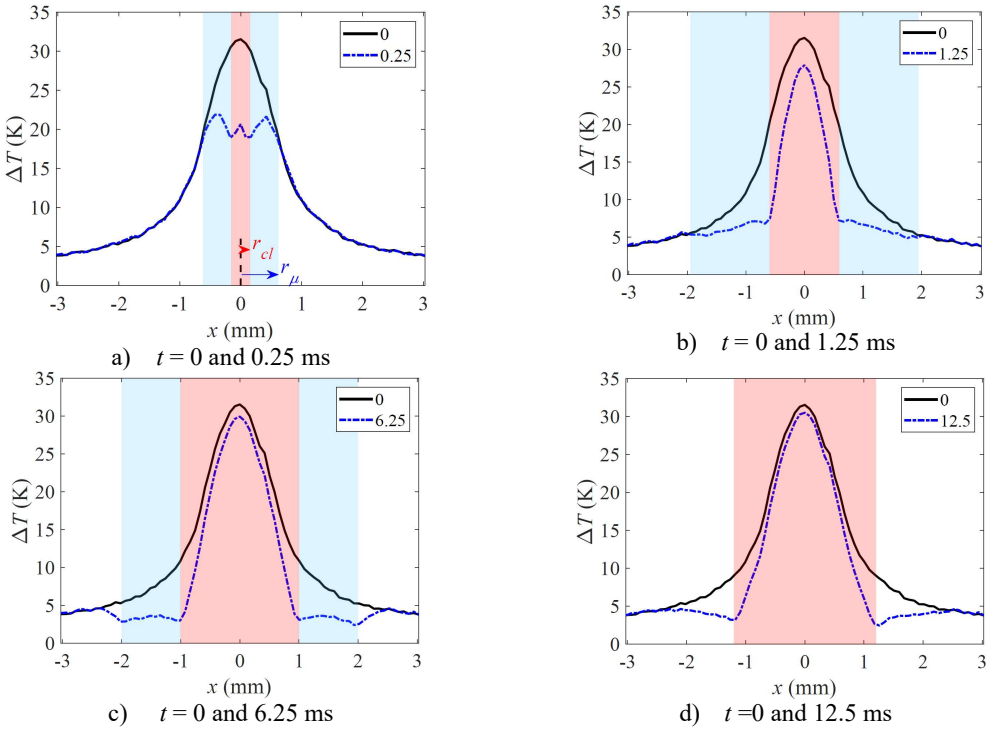

Figure 7. Spatial distributions $\Delta T(x)$ (blue dotted lines) for different time moments during the microlayer formation as compared to $\Delta T(x, t = 0)$ (black lines). The shaded areas represent the extents of dry spot (in rose) and of microlayer (in blue) in the sides.

5.5 Wall heat flux

Figure 8 shows the wall heat flux distribution $q_l(x, y)$ for t = 6.25 ms (corresponding to $\Delta T(x, y)$ of Fig. 6b). One can identify the dry spot on the wall as a nearly circular region with a very low q_l; the surrounding zone with high q_l corresponds to the microlayer. $q_l(x, y)$ follows a centrally symmetric pattern corresponding to the bubble shape. Similarly to the previous section, we consider the horizontal cut, i.e. the fluxes at $y = 0$. Figure 9 shows the time evolution of heat flux for each term in the RHS of Eq. (4) at x = 1.1 mm $\equiv r_d$, which corresponds to a ring on the wall where the microlayer disappears (radius where the curves r_μ and r_{cl} cross in Fig. 4a). We fix $y = 0$ for all the data described hereafter. One can see that q_a and q_d are negligible compared to q_p and j_0. This occurs because of the thinness of the ITO film, which provides a very small transverse cross-section area. Therefore, both the lateral heat diffusion and the heat capacity of ITO are tiny. At $t < 0.5$ ms, the point $r = r_d$ is in the contact with the liquid so only convection occurs, which provides a small heat exchange. q_p increases sharply at around 0.5 ms. At this instant, $r_\mu = r_d$ according to Fig. 4a, thus corresponding to the moment of formation of microlayer at $r = r_d$. Evaporation of microlayer causes a high heat transfer from the porthole towards the bubble, producing a sharp increase of q_p. It occurs because the porthole accumulates a big amount of heat between the nucleation events. During the microlayer evaporation at 0.5ms $\leq t \leq$ 12.5ms, q_p is the dominant contribution to q_l (roughly 90% at t = 0.5 ms and 75% at t =12 ms), much larger than the source term j_0.

At t = 12.5 ms, the receding contact line reaches the point r_d. At this particular position, ΔT is quite small so there is no heat transfer peak. For $t > 12.5$ ms, the contact line changes the motion direction (begins to advance, see Fig. 4a) so $r_{cl} < r_d$ and the microlayer vanishes. The point r_d comes to the contact with the bulk liquid again. The heat absorbed in the ITO is transferred to the porthole (negative q_p) because of its higher effusivity compared to liquid water. A similar trend is observed for other points along the heater. The only difference is the presence of the heat transfer peak at the instant where the contact line passes the point (in which case it happens at a positive local ΔT).

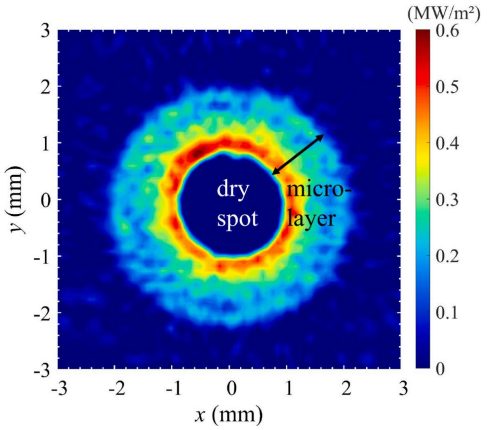

Figure 8. Heat flux spatial distribution $q_l(x, y)$ at t = 6.25 ms corresponding to that of temperature in Fig. 6b.

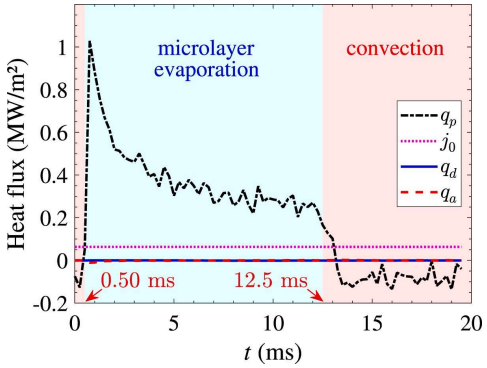

Figure 9. Contributions of different terms of Eq. (4) to the microlayer heat flux q_l at x =1.1 mm, y = 0 as functions of time.

Figures 10 depict q_l as functions of t for fixed x, and of x for a fixed t, respectively. In Fig.10a, q_l decreases over time due to the decrease of q_p at x =1.6 mm. In Fig. 10b, q_l also decreases with increasing x due to the nonuniform laser heating distribution on the wall. The maxima of $q_l(x)$ correspond to the contact line positions, which is a well-known phenomenon. One can see that the calculated heat flux in the dry spot is negative. This might be an artifact of calculation (resulting from the ill-posed problem) rather than a physical phenomenon. Such anomalies exist in previous flux reconstructions (Jung & Kim, 2014) where the heat flux in the dry spot was, on the contrary, anomalously large.

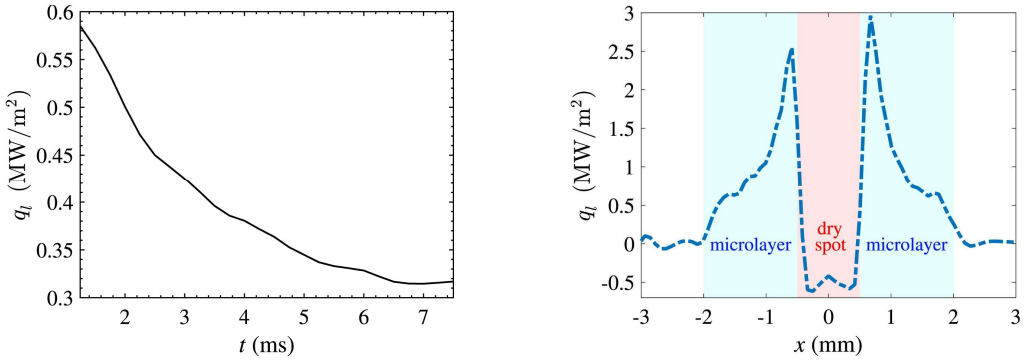

a) $q_l(t)$ determined with Eq. (4) at x = 1.6 mm. b) $q_l(x)$ at t = 1.25ms.

Figure 10. Temporal and spatial variations of the microlayer heat flux at y = 0.

The time evolution of the heat flux at the contact line $q_{l,cl}$ is shown in Fig. 11. It follows a quick decay at the initial stage of its receding (i.e. the outward motion). This occurs because the contact line recedes over the heater, the superheating of which decreases as the contact line moves away from the hot spot provided by the laser heating. The superheating ΔT_{cl} at the contact line is low and nearly constant for t > 5 ms until the end of the receding end so $q_{l,cl}$ is constant. For t > 12.5 ms, the contact line advances as the buoyancy pulls the bubble upward. $q_{l,cl}$ thus increases as the contact line moves back towards the center of the heated area. $q_{l,cl}$ is therefore highly dependent on ΔT_{cl}, with a maximum at the very early moments of its receding stage. It should be noted however that the discussed heat flux is actually smoothed over the pixel size (84 μm). The local heat flux at the contact line can thus be considerably higher as suggested by theoretical approaches (Nikolayev, 2022).

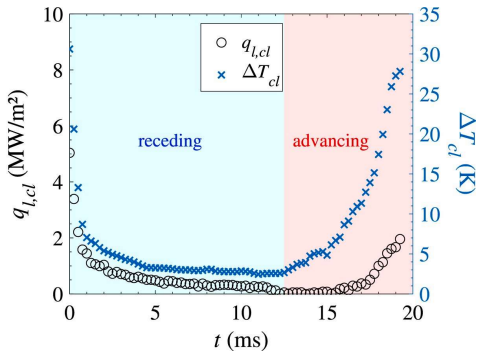

Figure 11. Time evolution of q_l and ΔT at the contact line.

5.6 Interfacial thermal resistance

By using Eq. (1), one can determine the interfacial thermal resistance R^i from the experimental data on ΔT, q_l, and δ. R^i can only be computed between t =1.25 and 7.5 ms where the δ data is available. Figure 12a displays the time evolution of R^i computed by using the data at two points at y = 0: x = 1.53 mm and 1.6 mm. The data shows an increase of R^i / R^i_{theo} over time and is compatible with the hypothesis $R^i = R^i_{theo}$ in the beginning of evolution. $R^i / R^i_{theo} = 10$ at t =1.25 ms and about 60 at t = 7.5 ms. One can fit the data with the simplest linear law

$$R^i / R^i_{theo} = Ct + 1, \tag{5}$$

where the parameter C = 7879 s^{-1} is determined with the least squares method (Fig. 12a). Such a temporal increase can be explained by accumulation of impurities present in water at the liquid-vapor interface during microlayer evaporation. The impurity accumulation at evaporation is well known in water (coffee stain effect (Parneix, *et al.*, 2010)). This effect appears here in spite of high water purity used for cell filling: it is difficult to avoid contamination by the cell itself; its cleaning before experiment is never ideal. Note that in our experiments, R^i is smaller than in two other experiments mentioned in Fig. 12a, which suggests that we worked with purer water.

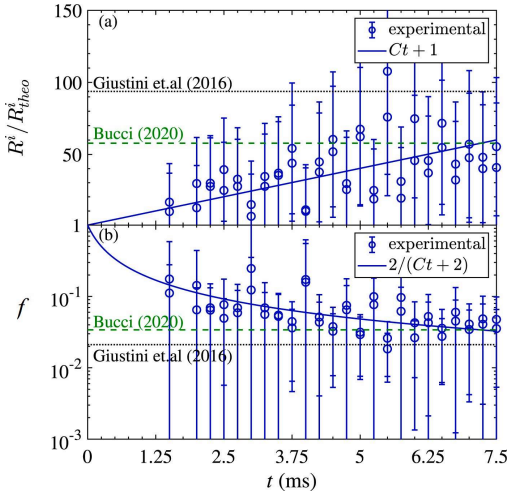

Figure 12. Temporal evolution of (a) R^i / R^i_{theo} and (b) accommodation coefficient f computed using Eq. (6). The data (Giustini, *et al.*, 2016; Bucci, 2020) are also shown.

Figure 12b shows the effect of the time dependence on f, the accommodation coefficient. By using Eq. (3), one can express f as a function of the ratio R^i / R^i_{theo},

$$f = \frac{2}{R^i / R^i_{theo} + 1}, \tag{6}$$

The fit corresponding to Eq. (6) is $f = 2/(Ct + 2)$. f decreases from about 0.2 at t = 1.25 ms down to 0.03 at t = 7.5 ms. Bucci (2020) obtained 0.03 on average while Giustini, *et al.*, (2016) finds that f can be as low as 0.02. In comparison with these similar experiments, the main outcome of our results is a clear indication of the time-dependence of R^i and f.

While the previous investigations lack the error analysis, we determine the uncertainties on the interfacial thermal resistance and accommodation coefficient (Fig. 12). The uncertainty on a unique R^i / R^i_{theo} data point is up to ±50 while on f it is up to ±0.4. Such large values come from the uncertainty of determination of the wall heat flux obtained from an intrinsically ill posed inverse problem. These difficulties are experienced by all teams working in this field. Better mathematical methods of heat flux reconstruction thus need to be developed in future studies.

To evaluate whether R^i is important for microlayer studies, one can compare it to the conductive thermal resistance $R^c = \delta(t) / k_l$ of the microlayer. Figure 13 depicts the time evolution of the ratio R^i / R^c for x = 1.53 mm and 1.6 mm at y = 0. The fit is based on Eq. (5). R^i / R^c increases from 0.1 at t =1.25 ms up to 0.5 at t = 7.5 ms. This occurs because R^i and R^c evolve differently over time. While R^i increases (Fig. 12a), R^c decreases because of microlayer evaporative thinning (Fig. 5). As a result, the ratio R^i / R^c can only increase which shows the importance of R^i for the microlayer studies and its theoretical modeling.

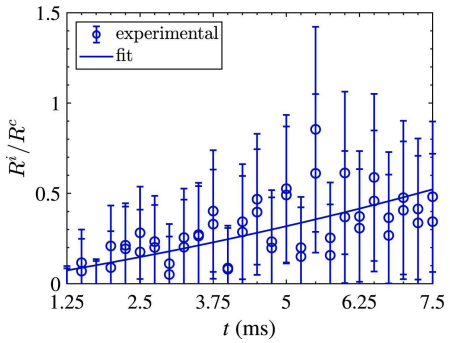

Figure 13. Time evolution of R^i / R^c.

6. CONCLUSION

We report experimental results on single bubble pool nucleate boiling at atmospheric pressure and saturation conditions. The experiments are performed with ultra-pure water. The near-wall heat transfer phenomena during the microlayer evaporation are analyzed with synchronous high-speed and high resolution optical techniques. White-light interferometry, infrared thermography and side-wise shadowgraphy are used to measure the microlayer thickness, wall temperature and bubble macroscopic shape, respectively. The wall heat flux is reconstructed numerically by solving an inverse problem. The nucleation and growth of a single bubble at a time are produced by heating with an infrared laser. In the present boiling study, we use an experimental technique (the white light interferometry) to measure the microlayer thickness with high precision (within nm) and high degree of confidence.

The microlayer is not completely evaporated. It disappears because its length vanishes (the contact line and the bubble edge approach each other). Therefore, the ‘’microlayer depletion’’ term does not seem appropriate; the term ‘’microlayer disappearance’’ is more adequate. This is a general feature; the same behavior is observed at uniform heating (Jung & Kim, 2015).

The spatio-temporal evolution of the wall temperature is analyzed. The contact line position can be determined as it presents a heat sink. Evaporation of microlayer works as an effective heat transfer bridge that cools the heated wall along the entire microlayer extent. Our results show that despite high wall temperature gradients existing prior to the bubble nucleation, the microlayer evaporation is able to both cool the wall rapidly and homogenize its temperature.

The spatio-temporal evolution of the wall heat flux is reconstructed. Its partition shows that the major part of heat used for the bubble growth comes from the energy accumulated in the massive heater during the waiting time rather than from the direct heating.

We determine the thermal resistance of the vapor-liquid interface and reveal its increase over time while the microlayer evaporates. Our results are compatible with the hypothesis that in the beginning of evaporation, the interfacial thermal resistance is close to the theoretical value provided by the kinetic evaporation theory with the unity

accommodation coefficient. During the bubble growth, the interfacial thermal resistance increases about 60 times. One can guess that this occurs due to progressive accumulation of impurities at the liquid-vapor interface, which is a well-known phenomenon for water. The results indicate that the interfacial thermal resistance is comparable to the conductive resistance of the microlayer, which shows its importance and necessity of its account in future numerical simulations of water boiling heat transfer. The determination of the interfacial thermal resistance is based on a numerical reconstruction of the wall heat flux. This is an ill-posed problem, the direct solution of which exhibits large fluctuations. A better method of heat flux reconstruction thus needs to be used in future to provide a better analysis of the interfacial thermal resistance.

The experimental data provided here are relevant to the understanding of the fundamental aspects of near-wall heat transfer phenomena in the presence of microlayer. Our data can be used to validate new numerical models of boiling.

7. REFERENCES

Bucci, M., 2020. A theoretical and experimental study of vapor bubble dynamics in separate effect pool boiling conditions*,* Master's thesis, University of Pisa, Italy.

Bureš, L. & Sato, Y., 2021. On the modelling of the transition between contact-line and microlayer evaporation regimes in nucleate boiling. *J. Fluid Mech.,* Volume 916, p. A53.

Bureš, L. & Sato, Y., 2022. Comprehensive simulations of boiling with a resolved microlayer: validation and sensitivity study. *J. Fluid Mech.,* Volume 933, p. A54.

Chen, Z. & Utaka, Y., 2015. On heat transfer and evaporation characteristics in the growth process of a bubble with microlayer structure during nucleate boiling. *Int. J. Heat Mass Transf.,* Volume 81, pp. 750-759.

Eames, I. W., Marr, N. J. & Sabir, H., 1997. The evaporation coefficient of water: a review. *Int. J. Heat Mass Transfer,* Volume 40, pp. 2963-2973.

Fourgeaud, L. *et al*., 2016. Evaporation-driven dewetting of a liquid film. *Phy. Rev. Fluids,* Volume 1, p. 041901(R).

Giustini, G., 2024. Hydrodynamic analysis of liquid microlayer formation in nucleate boiling of water. *Int. J. Multiphase Flow,* Volume 172, p. 104718.

Giustini, G., 2024. Hydrodynamic analysis of liquid microlayer formation in nucleate boiling of water. *Int. J. Multiphase FLow,* Volume 172, p. 104718.

Giustini, G. *et al*., 2019. Microlayer evaporation during steam bubble growth. *Int. J. Therm. Sci.,* Volume 137, pp. 45-54.

Giustini, G., Jung, S., Kim, H. & Walker, S. P., 2016. Evaporative thermal resistance and its influence on microscopic bubble growth. *Int. J. Heat Mass Transfer,* Volume 101, pp. 733-741.

Guion, A., Afkhami, S., Zaleski, S. & Buongiorno, J., 2018. Simulations of microlayer formation in nucleate boiling. *Int. J. Heat Mass Transfer,* Volume 127, pp. 1271-1284.

Guion, A., Afkhami, S., Zaleski, S. & Buongiorno, J., 2018. Simulations of microlayer formation in nucleate boiling. *Int. J. Heat Mass Transfer,* Volume 127, pp. 1271-1284.

Jung, S. & Kim, H., 2014. An experimental method to simultaneously measure the dynamics and heat transfer associated with a single bubble during nucleate boiling on a horizontal surface. *Int. J. Heat Mass Transfer,* Volume 73, pp. 365-375.

Jung, S. & Kim, H., 2014. An experimental method to simultaneously measure the dynamics and heat transfer associated with a single bubble during nucleate boiling on a horizontal surface. *Int. J. Heat Mass Transfer,* Volume 73, pp. 365-375.

Jung, S. & Kim, H., 2015. An experimental study on heat transfer mechanisms in the microlayer using integrated total reflection, laser interferometry and infrared thermometry technique. *Heat Transf. Eng.,* Volume 36, pp. 1002-1012.

Marek, R. & Straub, J., 2001. Analysis of the evaporation coefficient and the condensation coefficient of water. *Int. J. Heat Mass Transf.,* Volume 44, pp. 39-53.

Myers, J. G. *et al*., 2005. Time and space resolved wall temperature and heat flux measurements during nucleate boiling with constant heat flux boundary conditions. *Int. J. Heat Mass Transf.,* Volume 48, pp. 2429-2442.

Nikolayev, V. S., 2022. Evaporation effect on the contact angle and contact line dynamics. In: M. Marengo & J. De Coninck, eds. *The Surface Wettability Effect on Phase Change.* s.l.:Springer, pp. 133-187.

Parneix, C. *et al*., 2010. Dips and rims in dried colloidal films. *Phys. Rev. Lett.,* Volume 105, p. 266103.

Surtaev, A. *et al*., 2018. An experimental study of vapor bubbles dynamics at water and ethanol pool boiling at low and high heat fluxes. *Int. J. Heat Mass Transf.,* Volume 126, pp. 297-311.

Tecchio, C., 2022. *Experimental study of boiling: Characterization of near-wall phenomena and bubble dynamics,* Ph.D thesis, Université Paris-Saclay, France.

Tecchio, C. *et al*., 2024. Microlayer evaporation during bubble growth in nucleate boiling. *Int. J. Heat Mass Transf.,* Volume 231, p. 125860.

Tecchio, C. *et al*., 2022. *Microlayer dynamics at bubble growth in boiling. Proc. 16th Int. Conf. Heat Transf. Fluid Mech. Thermodynamics (HEFAT-ATE 2022)*, pp. 624-629.

Tecchio, C. *et al*., 2024. Microlayer in nucleate boiling seen as Landau-Levich film with dewetting and evaporation. *J. Fluid Mech.*. doi: 10.1017/jfm.2024.488

Torres, L., Urbano, A., Colin, C. & Tanguy, S., 2024. On the coupling between direct numerical simulation of nucleate boiling and a micro-region model at the contact line. *J. Comput. Phys.,* Volume 497, p. 112602.

Urbano, A., Tanguy, S., Huber, G. & Colin, C., 2018. Direct numerical simulation of nucleate boiling in micro-layer regime. *Int. J. Heat Mass Transfer,* Volume 123, pp. 1128-1137.

Urbano, A., Tanguy, S., Huber, G. & Colin, C., 2018. Direct numerical simulation of nucleate boiling in micro-layer regime. *Int. J. Heat Mass Transfer,* Volume 123, pp. 1128-1137.

Utaka, Y., Hu, K., Chen, Z. & Morokuma, T., 2018. Measurement of contribution of microlayer evaporation applying the microlayer volume change during nucleate pool boiling for water and ethanol. *Int. J. Heat Mass Transf.,* Volume 125, pp. 243-247.

Utaka, Y., Kashiwabara, Y., Ozaki, M. & Chen, Z., 2014. Heat transfer characteristics based on microlayer structure in nucleate pool boiling for water and ethanol. *Int. J. Heat Mass Transf.,* Volume 68, pp. 479-488.

Zhang, X. & Nikolayev, V. S., 2022. Dewetting acceleration by evaporation. *J. Fluid Mech.,* Volume 948, p. A49.